Direct investigation of anisotropic suspension structure in pressure-driven flow

C. Gao,[1] S. D. Kulkarni,[2] J. F. Morris,[2] and J. F. Gilchrist[1,*]
[1]*Department of Chemical Engineering, Lehigh University, Bethlehem, Pennsylvania 18015, USA*
[2]*Benjamin Levich Institute and Department of Chemical Engineering, The City College of New York, New York, New York 10031, USA*
(Received 20 July 2009; published 15 April 2010)

Evidence is presented to show the microstructural anisotropy responsible for normal stress in sheared suspensions. Particle velocimetry is combined with three-dimensional particle locations obtained via confocal microscopy at rest. A range of volume fractions ϕ and local shear rates $\dot{\gamma}$ are investigated in a weakly Brownian pressure-driven suspension. At high $\dot{\gamma}$, the pairwise distribution shows a strong probability along the axis of compression similar to observations from Stokesian dynamics simulation at $\phi=0.32$. At the channel center where $\dot{\gamma}\rightarrow 0$, the concentrated suspension at $\phi=0.56$ behaves as a confined isotropic fluid.

DOI: 10.1103/PhysRevE.81.041403 PACS number(s): 82.70.Kj, 47.57.J−, 47.57.E−

The shearing of suspensions with moderate to high particle volume fractions is known to generate normal stresses [1–3]. This force primarily acts orthogonal to the direction of flow and is generally believed to be a result of multiparticle hydrodynamic interactions. The normal stresses may be interpreted as the tendency to dilate under deformation; when constrained to a fixed volume, dilation does not occur but the normal stresses are measurable. Rheological measurement of these normal stresses is challenging because the normal stresses are small until approaching jamming at high solid volume fractions; however, recent macroscopic measurements in Couette flow have succeeded in measuring osmotic pressure [4]. In the presence of nonlinear shear fields, these normal stresses result in the migration of particles [5], which demixes suspensions. The development of constitutive equations to describe this behavior in a wide range of flows has been slow due to the fact that these normal stresses are the result of subtle structural anisotropies. Detailed three-dimensional (3D) particle-level information from a single experiment is necessary in order to identify local structure. The development of a fundamental understanding of these multiparticle hydrodynamic interactions will impact a suspension process design for mixing, separations, and transport and will facilitate a deeper understanding of natural processes including sediment transport and blood flow.

Brownian and non-Brownian systems ranging in volume fraction $0.3<\phi<0.5$ have been studied extensively through theory and simulations to identify and understand the effect of shear-induced microstructural anisotropies on the development of normal stresses. Stokesian dynamics simulations [6,7] predict a higher correlation of nearest-neighbor interactions along the compressive axes of the flow in the $\mathbf{v}-\nabla\mathbf{v}$ projection of the pair distribution function, $g(\mathbf{r})$. From an isotropic state, these dynamics develop quickly with the onset of flow [8]. While the normal stresses disappear upon the cessation of flow in non-Brownian systems, the structural anisotropy is preserved [8,9]. This anisotropy is destroyed upon the reversal of the flow direction and re-emerges oriented relative to the new flow direction [8]. This connection between local structural anisotropy and discontinuities observed upon flow reversal was confirmed by direct imaging of experiments exhibiting this fore-aft asymmetry [10] but experiments to date lack the detail available via simulation. For $\phi>0.5$, shear deformation results in a higher degree of local order including particle chaining and crystallization [11].

We present measurements of 3D particle-level anisotropy generated from shear in a pressure-driven flow using confocal laser scanning microscopy (CLSM). The advantage of this technique is that direct 3D imaging gives data that can be directly compared to simulation and probed using a multitude of analyses. We used monosized suspensions of $2a=1.01$ μm diameter SiO_2 microspheres at a bulk volume fraction $\phi_{bulk}=0.41$ in 3:1 glycerol:water with 0.1 mM Rhodamine-B fluorescent index-matching solution. To minimize electrostatic interactions in order to predominantly study the result of hydrodynamic interactions, we added NaOH and NaCl to adjust the *p*H to 8.0 and the screening length to $\kappa^{-1}=1.5$ nm. We introduce this suspension into a 50 mm$\times$40 μm$\times$100 μm microchannel at a pressure drop as high as 1 atm using compressed nitrogen. The coordinates (x, y, and z) that represent the ($\mathbf{v}$, $\nabla\mathbf{v}$, and $\nabla\times\mathbf{v}$) directions are reported as dimensionless quantities scaled by the 20 μm half-height of the channel in the $\nabla\mathbf{v}$ direction. The nonlinear shear gradient as a result of pressure-driven flow induces significant suspension migration. The final steady volume fraction profile ϕ far from the entrance, shown in Fig. 1(a), is higher at the center and lower near the walls. The local viscosity depends on the local volume fraction; therefore, the velocity profile deviates from axial Poiseuille flow of a Newtonian fluid. Fully developed far from the entrance region, this generates a velocity profile across the y direction at the center having a roughly 1 mm/s center velocity, plotted in Fig. 1(b). For comparison axial Poiseuille flow of a Newtonian fluid, as calculated using the solution derived in [11], is also shown in Fig. 1(b). The local shear rate $\dot{\gamma}$, calculated from the local slope of the velocity profile over measured values within the nearest 6 μm of each point, is nearly linear and is used to define the local Péclet number, $\mathrm{Pe}\equiv 6\pi\eta_0\dot{\gamma}a^3/(kT)$, where η_0 is the fluid viscosity and kT is the thermal energy. The nonlinear velocity profile as a result of pressure-driven flow creates shear rate variation in the z direction as well; however, as we are considering only the

*gilchrist@lehigh.edu

 ©2010 The American Physical Society

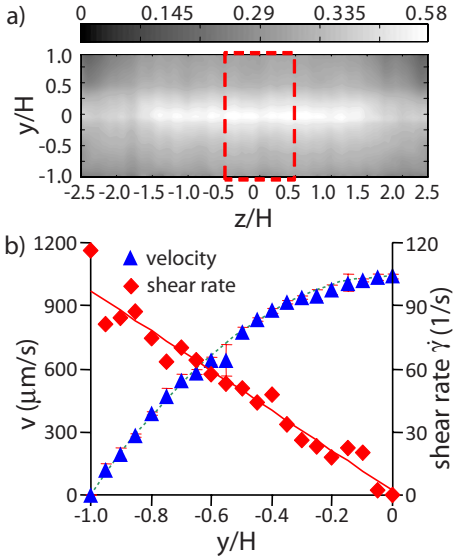

FIG. 1. (Color online) (a) The particle volume fraction profile transverse to the direction of flow and the region of interest where data are sampled after stopping the flow. (b) The measured velocity profile in the region of interest (triangles) and the parabolic profile (green dotted line) for comparison. The shear rate profile calculated from the velocity in y axis (diamonds) fit with a linear trend line (red solid line).

small central portion (20% of the overall z width), the shear rate deviation in this direction can be neglected.

Dynamic confocal laser scanning microscopy (VTeye, Visitech Int.) allows single plane particle tracking for velocimetry to measure velocity profiles as well as measurement of particle concentration patterns in the plane transverse to the direction of flow [12,13]; however, its scanning speed is insufficient to track fast moving particles in 3D space and enable investigations of the microstructure. To eliminate transients, after flowing for 10 min we quickly stop the flow, similar to [14], and scan the entire depth of the channel in the $\nabla\mathbf{v}$ direction within a region of interest (ROI) located at the midpoint at the center of the $\nabla\times\mathbf{v}$ direction ($20\times40\times20$ $\mu\mathrm{m}^3$). The use of compressed nitrogen gives a stable driving pressure and the fast pressure release using a three-way valve near the channel entrance allows a rapid arrest of suspension flow without flow reversal. In non-Brownian density-matched systems, the structure that produces normal stresses is preserved upon the cessation of the flow provided the flow does not reverse [8,9]. After suspension flow stops, the ROI is scanned at high speed of $\sim$10 pixels/μm over 2.4 s and the 3D locations of particles within are identified [15,16]. Fast scanning allows identification of particle locations before significant Brownian diffusion and sedimentation alter the local structure. Multiple scans are obtained and the insignificant Brownian and buoyant drift that occurs in the time between scans suggests that the structure is unaltered in the duration of a single scan. The average particle number density $\bar{n}=N/V$ is used to calculate the local volume fraction as $\phi=\bar{n}\frac{4}{3}\pi r^3$; this provides accurate particle density measurements [Fig. 2(a)] that match well with measurements taken during the flow.

With the particle locations, local coordination can be used

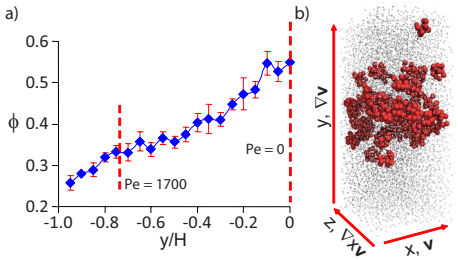

FIG. 2. (Color online) (a) Density profile across the ROI from 3D particle locations shows the result of migration. (b) Rendering of experimentally obtained particle locations as small gray points and true to scale larger red particles for those particles having FCC or HCP bond order.

to investigate the suspension structure. A representative 3D reconstruction of the particles found in the ROI is shown in Fig. 2(b). The particles are size and color coded to distinguish disordered particles (1/5th size and gray) from those having local face-centered-cubic (FCC) or hexagonal-close-packed (HCP) structure or neighbors thereof (red and rendered to scale), as defined in previous investigation of the structure of liquids by identifying bond order parameters based on bond angle weighted averages [17]. Most ordered particles are located near the center, where they comprise roughly 20% of particles in the region $-0.25\leq y/H\leq0.25$. The generation of crystalline order in coexistence with a liquid structure is expected for an equilibrium dispersion (i.e., Pe=0) for $0.494<\phi<0.545$.

Using the accelerated Stokesian dynamics technique [18] with Brownian motion [19], we simulate the motion of colloidal particles suspended in sheared viscous fluid in the limit of zero particle inertia where viscous effects are dominant. For a system of N particles suspended in an incompressible Newtonian fluid, fluid motion is governed by the Stokes equations while particle motion is described by the N-body Langevin equation; this equation is integrated to obtain time evolution of the particle positions, as detailed in Refs. [18,19]. The simulations are performed using periodic boundary conditions in all directions with Lees-Edwards boundary conditions for shear flow [20]. Results reported here use $N=512$ particles in the simulated unit cell. The bulk simple shear flow is $\mathbf{u}=(u_x,u_y,u_z)=(\dot{\gamma}y,0,0)$, so that x-y is the plane of shear and y-z is the plane perpendicular to the mean flow.

The particle configurations, obtained experimentally and in simulations by varying the sampling location within the channel and Pe, respectively, are used to determine the pair distribution function, $g(\mathbf{r})=P_{1|1}(\mathbf{r})/\bar{n}$. $P_{1|1}(\mathbf{r})$ is the probability of finding a particle at position $\mathbf{r}$ given a particle centered at the origin. To compare with the experimental data, $g(\mathbf{r})$ is evaluated in different planes. For example, $g(x,y)$ defines $g(\mathbf{r})$ within the shear plane. To calculate $g(x,y)$ we consider all pair separations in which the magnitude of the z component of the separation satisfies $r_z<2a$. Experimentally, the data are averaged over five experiments. Simulations average a sufficiently large number of configurations that the result becomes independent of the number of configurations [7,21]. The pair distribution $g(x,y)$ is evaluated from a histogram of

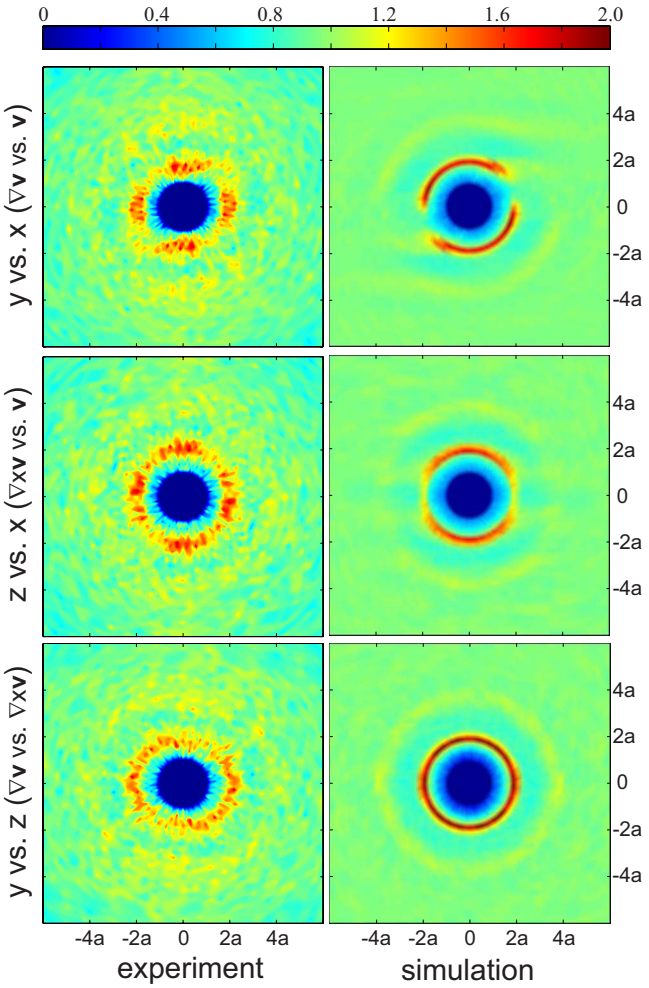

FIG. 3. (Color online) Experimental compilation (left) and Stokesian dynamics (right) simulations of local pair distribution functions. Pair distribution functions $g(x,y)$ (first row), $g(x,z)$ (second row), and $g(z,y)$ (third row) located at $-0.85 \leq y/H \leq -0.65$, $\phi=31.9\%$, Pe=1700 in the channel and simulated at Pe=1700.

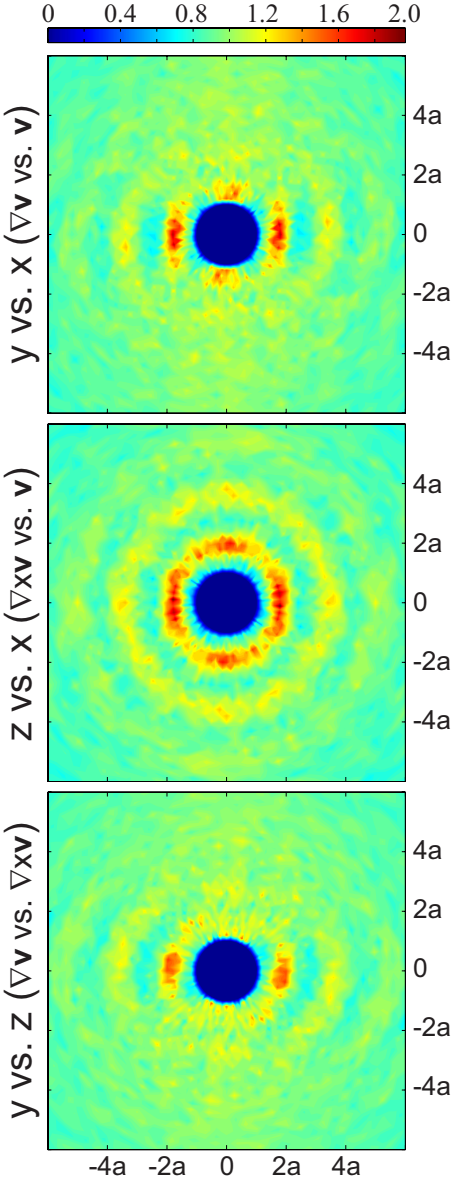

FIG. 4. (Color online) Experimental compilation of local pair distribution functions $g(x,y)$ (first row), $g(x,z)$ (second row), and $g(z,y)$ (third row) located at $-0.1 \leq y/H \leq 0.1$, $\phi_{local}=56.4\%$, Pe =0.

pair separation vectors in the bins normalized by the respective bin volume ($\Delta r=0.2a$ and $\Delta\theta=3.6°$). The distributions $g(z,y)$ and $g(x,z)$ are evaluated in the same fashion. All plots of $g(\mathbf{r})$ span dark blue to red colors representing the range $0 \leq g(\mathbf{r}) \leq 2$.

In Fig. 3, the pair distribution functions measured and calculated at Pe=1700 are seen to have a central region of particle exclusion. As a result of the way the data are represented, symmetry through the origin is mandatory in all pair distribution functions. For $g(x,y)$ representing the shear-plane structure, inside $r<2a$ a strong pair correlation exists in the compressional region near the line $x=-y$ and less in the extensional region neighboring a particle. This appears at $r<2a$ due to the way the out-of-plane data are projected. In the simulation, the near-contact peak is similar to that found in previous studies [6,7] and is the primary microstructural generator of macroscopic normal stresses. This peak deviates from the experimental measurement in that the correlation is less uniform in the θ direction and, in particular, is stronger along the x and y axes. The shape of the wake is different in the extensional region, and there is a stronger correlation along the x axis in the experimental results. In both experiments and simulations, a second peak just inside $r=4a$ is apparent but a direct comparison of the structural details is difficult due to the weakness of correlation in this region and the resulting lower signal-to-noise ratio.

In $g(x,z)$ for the microstructure in the velocity-vorticity plane, the fore-aft symmetry apparent in the simulations is not found experimentally. We hypothesize that the shear gradient along the z direction, $\dot{\gamma}_z$, in the experiment is nonzero even though measurements are near $z=0$ and are significant enough to create similar increased correlation along the compressional region. In the first ring of higher probability inside $r=2a$, simulations show lower correlation in the x direction near $z=0$ that results from averaging the $g(x,y)$ data. This same projection for the experimental data results in higher

pairwise probability in the x direction near $z=0$ and lower probability along the $x=y$ and $x=-y$ directions. A second ring of higher probability is found again inside $r=4a$ for both experiments and simulations. In the vorticity-shear gradient plane where flow goes into the plane of the page for the experiment, there are first- and second-order rings of higher probability in the pair distribution function $g(z,y)$ as found in the other two planes. There are also dissimilarities, where simulations predict near uniformity in probability in the angular direction, the experiments show slightly higher probability in the shear plane in the vorticity direction.

The pair distribution functions are also reported for the center of the channel $-0.1<y/H<0.1$ where the local volume fraction peaks at $\phi=0.564$ (Fig. 4). At this volume fraction the suspension is expected to generate crystalline order at equilibrium. Likewise, crystallization has been shown in the presence of shear at similar volume fractions [8,22–25]. At this point in the channel, although the concentration gradients driven by shear migration are assumed to be well established, particles near the center only spend roughly 30 s in the microchannel; it is unlikely that the suspension has reached equilibrium in this weakly Brownian suspension. This, plus consideration of any residual shear in either the y or z direction, may be the reason why only a fraction of particles near the center of the channel rendered in Fig. 2 are found to have local order. The velocity-vorticity plane $g(x,z)$ displays three clear rings of higher pairwise probability just inside $r=2a$, $r=4a$, and $r=6a$, and arguably a fourth near the corners at $r=8a$. In the nearest-neighbor ring, there is some variation in probability in the angular direction with the highest probability along the axes and the lowest along $x=y$ and $x=-y$. The observations in the pairwise distributions in the alternate planes $g(x,y)$ and $g(z,y)$ show little correlation outside the x-z plane with the exception of higher probability in the nearest-neighbor pair in $g(x,y)$ along the y axis. This anisotropy suggests that if crystallization does occur, it will be nucleated and propagate in the x-z plane.

In conclusion, CLSM-enabled 3D measurement of particle locations in experiments enables a direct microstructure comparison to particle locations generated by Stokesian dynamics simulations. The apparent anisotropies lead to shear migration in nonlinear velocity profiles that enable probing of various Pe's and ϕ's in a single experiment. Experimental and simulated pair distribution functions largely agree, although the details deviate possibly due to the lateral confinement of the suspension in the z direction. This flow-arresting technique can be expanded to probe the structure of any hydrodynamic-dominated nonkinetic or weakly kinetic suspension to probe heterogeneities that result from polydispersity, particle shape anisotropy, and some non-Newtonian fluids comprising the continuous phase in a wide range of flows.

The authors want to thank J. Brady for insightful conversations and E. Weeks for the 3D particle tracking algorithms. The microfabrication was performed at the Cornell NanoScale Facility. This material is based upon work supported by the National Science Foundation under Grant No. 0630191 (J.F.G.), funding from the ACS Petroleum Research Fund (J.F.G. and J.F.M.), and North American Mixing Forum (J.F.G.).

[1] J. J. Stickel and R. L. Powell, Annu. Rev. Fluid Mech. **37**, 129 (2005).
[2] J. F. Morris and F. Boulay, J. Rheol. **43**, 1213 (1999).
[3] I. E. Zarraga, D. A. Hill, and D. T. Leighton, J. Rheol. **44**, 185 (2000).
[4] A. Deboeuf, G. Gauthier, J. Martin, Y. Yurkovetsky, and J. F. Morris, Phys. Rev. Lett. **102**, 108301 (2009).
[5] C. J. Koh, P. Hookham, and L. G. Leal, J. Fluid Mech. **266**, 1 (1994).
[6] D. R. Foss and J. F. Brady, J. Fluid Mech. **407**, 167 (2000).
[7] J. F. Morris and B. Katyal, Phys. Fluids **14**, 1920 (2002).
[8] J. J. Stickel, R. J. Phillips, and R. L. Powell, J. Rheol. **51**, 1271 (2007).
[9] V. G. Kolli, E. J. Pollauf, and F. Gadala-Maria, J. Rheol. **46**, 321 (2002).
[10] F. Parsi and F. Gadala-Maria, J. Rheol. **31**, 725 (1987).
[11] R. J. Butera, M. S. Wolfe, J. Bender, and N. J. Wagner, Phys. Rev. Lett. **77**, 2117 (1996).
[12] C. Gao, B. Xu, and J. F. Gilchrist, Phys. Rev. E **79**, 036311 (2009).
[13] C. Gao and J. F. Gilchrist, Phys. Rev. E **77**, 025301(R) (2008).
[14] D. Dendukuri, S. S. Gu, D. C. Pregibon, T. A. Hatton, and P. S. Doyle, Lab Chip **7**, 818 (2007).
[15] Using IDL code developed by Eric Weeks at Emory University using algorithms developed by Crocker and Grier [16].
[16] J. C. Crocker and D. G. Grier, J. Colloid Interface Sci. **179**, 298 (1996).
[17] P. J. Steinhardt, D. R. Nelson, and M. Ronchetti, Phys. Rev. B **28**, 784 (1983).
[18] A. Sierou and J. F. Brady, J. Fluid Mech. **448**, 115 (2001).
[19] A. J. Banchio and J. F. Brady, J. Chem. Phys. **118**, 10323 (2003).
[20] M. Allen and D. Tildesley, *Computer Simulation of Liquids* (Oxford University Press, New York, 1987).
[21] S. D. Kulkarni and J. F. Morris, J. Rheol. **53**, 417 (2009).
[22] R. L. Hoffman, J. Rheol. **16**, 155 (1972).
[23] L. B. Chen, M. K. Chow, B. J. Ackerson, and C. F. Zukoski, Langmuir **10**, 2817 (1994).
[24] R. M. Amos, J. G. Rarity, P. R. Tapster, T. J. Shepherd, and S. C. Kitson, Phys. Rev. E **61**, 2929 (2000).
[25] P. Holmqvist, M. P. Lettinga, J. Buitenhuis, and J. K. G. Dhont, Langmuir **21**, 10976 (2005).